

Phase diagram of a three-dimensional antiferromagnet with random magnetic anisotropy

Felio A. Perez,^{*} Pavel Borisov, Trent A. Johnson, Tudor D. Stanescu, and David Lederman[†]

Department of Physics and Astronomy,

West Virginia University, Morgantown, WV 26506-6315, USA

M. R. Fitzsimmons

Los Alamos National Laboratory, Los Alamos, NM 87545, USA

Adam A. Aczel and Tao Hong

Quantum Condensed Matter Division, Neutron Sciences Directorate,

Oak Ridge National Laboratory, Oak Ridge, TN 37831, USA

(Dated: May 18, 2022)

Abstract

Three-dimensional (3D) antiferromagnets with random magnetic anisotropy (RMA) experimentally studied to date do not have random single-ion anisotropies, but rather have competing two-dimensional and three-dimensional exchange interactions which can obscure the authentic effects of RMA. The magnetic phase diagram $\text{Fe}_x\text{Ni}_{1-x}\text{F}_2$ epitaxial thin films with true random single-ion anisotropy was deduced from magnetometry and neutron scattering measurements and analyzed using mean field theory. Regions with uniaxial, oblique and easy plane anisotropies were identified. A RMA-induced glass region was discovered where a Griffiths-like breakdown of long-range spin order occurs.

PACS numbers: 75.30.Kz, 75.50.Ee, 75.10.Hk, 75.70.-i, 71.23.-k

The behavior of insulating antiferromagnets (AFs) can range from spin glass phases to random exchange, random anisotropy, and random field Ising models [1]. As a consequence, these compounds have received much attention due to their use as possible experimental realizations [2, 3] of theoretical models [4–6] for random magnets. Although AFs with pseudo random magnetic anisotropy (RMA) have been studied previously in $\text{Fe}_x\text{Co}_{1-x}\text{Cl}_2$, $\text{Fe}_x\text{Co}_{1-x}\text{Br}_2$, $\text{Fe}_x\text{Co}_{1-x}\text{TiO}_3$, and $\text{K}_2\text{Co}_x\text{Fe}_{1-x}\text{F}_4$ alloys, these systems only have approximate three-dimensional (3D) order because the effective RMA actually consists of different intra- and inter-layer magnetic exchange coupling constants [2, 3, 7–12]. To see why this is important, consider the spin Hamiltonian

$$H = \sum_i D (S_i^z)^2 + \sum_{ij} \Delta J_{ij} S_i^z S_j^z + \sum_{ij} J_{ij} \mathbf{S}_i \cdot \mathbf{S}_j, \quad (1)$$

where D is a single-ion anisotropy constant, ΔJ_{ij} is the difference between intra- and inter-layer exchange coupling constants, and J_{ij} is the intra-layer exchange coupling constant. In the mean field approximation, and taking into account only strongest neighbor interactions J , the Hamiltonian for a spin on the λ sublattice of an antiferromagnet becomes

$$H_\lambda = D (S_\lambda^z)^2 + z \Delta J S_\lambda^z \langle S_\lambda^z \rangle + z J \mathbf{S}_\lambda \cdot \langle \mathbf{S}_\lambda \rangle, \quad (2)$$

where z is the number of neighbors located on the sublattice $\bar{\lambda}$ that interact with a spin S_λ . The second term on the right hand side of Eq. 2, associated with an effective single-ion magnetic anisotropy resulting from the anisotropic exchange interaction, is strongly temperature dependent near the Néel temperature T_N because $\langle S_i^z \rangle \rightarrow 0$ as $T \rightarrow T_N$. On the other hand, the first term, which represents a true single-ion anisotropy, is not temperature dependent and therefore dominates the physics in the vicinity of the magnetic phase transition. Consequently, the physics that governs a system with true random single-ion anisotropy near the phase transition will be in general different from the physics generated by an effective RMA produced by anisotropic exchange interactions. In this Letter, we report on the phase diagram of a solid solution of two tetragonal 3D AFs that have orthogonal anisotropies originating solely from the single-ion anisotropies of each component, and thus represents a true 3D RMA antiferromagnet.

FeF_2 and NiF_2 share the rutile crystal structure with similar lattice parameters ($a = b = 4.6974 \text{ \AA}$ $c = 3.3082 \text{ \AA}$ for FeF_2 and $a = b = 4.6501 \text{ \AA}$ $c = 3.0835 \text{ \AA}$ for NiF_2 at room temperature) [13, 14]. Both materials are 3D AFs with similar exchange interaction

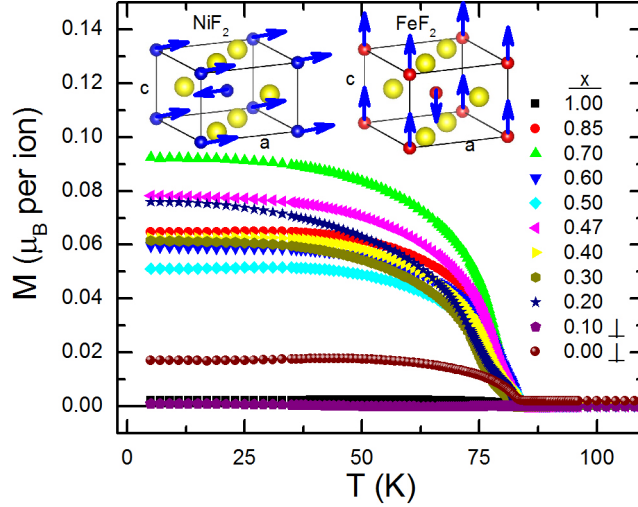


FIG. 1. TRM for $\text{Fe}_x\text{Ni}_{1-x}\text{F}_2$ samples measured in $H = 0$ after field cooling in $H_{FC} = 100$ Oe. Data for $x = 0$ and 0.10 were measured with H_{FC} perpendicular to the c -axis; all others measured with H_{FC} parallel to the c -axis. Inset: magnetic and crystalline structures of the parent compounds NiF_2 and FeF_2 . Yellow, blue, and red dots are F^+ , Ni^{2+} , and red Fe^{2+} ions, respectively.

strengths $zJS(S+1)/3$ and thus they have similar T_{NS} , 73.2K and 78.4K, for NiF_2 and FeF_2 , respectively [15, 16]. Their magnetic anisotropies are, however, very different. FeF_2 has a strong uniaxial anisotropy which results in its magnetic moments being aligned along the tetragonal c -axis, and is therefore considered an ideal realization of the 3D Ising model [16]. In NiF_2 , moments order antiferromagnetically in the a - b plane (Fig. 1) and are canted by $\approx 0.4^\circ$ with respect to the a - or b -axis [15]. Weak ferromagnetism in NiF_2 is due to the presence of two non-equivalent magnetic sites in the NiF_2 crystal lattice [17]. The similarity of crystal structures and magnetic exchange interactions in NiF_2 and FeF_2 suggests that $\text{Fe}_x\text{Ni}_{1-x}\text{F}_2$ is an ideal system to study RMA, which should vary from transition metal site to site depending on whether it is occupied by Ni^{2+} (favoring a - b plane ordering) or Fe^{2+} (favoring c -axis ordering) [18, 19].

In order to study the 3D RMA anisotropy problem, epitaxial (110) $\text{Fe}_x\text{Ni}_{1-x}\text{F}_2$ films were grown with nominal thicknesses of 37 and 100 nm on (110) MgF_2 substrates at 300 °C via molecular beam epitaxy, as described previously [18, 20], and capped with a 10 nm BaF_2 or Pd layer to prevent oxidation. The Fe concentration x was determined using a quartz-crystal monitor with an accuracy of ± 0.05 [18, 20]. Thermal remanent magnetization (TRM) measurements were carried out which consisted measuring the magnetization M while increasing

T from $T = 5$ K after field-cooling (FC) from $T = 300$ K in a field $H_{FC} = 100$ Oe (Fig. 1) along the in-plane $[001]$ (c-axis) and $[\bar{1}10]$ directions. The transition temperatures were determined by fitting the data near the phase transition with a rounded power-law

$$I = \frac{I_0}{\sigma_c \sqrt{2\pi}} \int_0^\infty (1 - T/T'_c)^\beta e^{-(T_c - T'_c)^2 / 2\sigma_c^2} dT'_c, \quad (3)$$

where T_c is a transition temperature, β is a critical exponent, σ_c is the width of the transition, and I_0 is an overall scaling factor [21, 22]. Magnetic hysteresis loops were measured as a function of T and found to have large coercivities at low T that decreased with increasing T for $0.2 < x < 1$, in agreement with previous measurements of $\text{Fe}_x\text{Ni}_{1-x}\text{F}_2/\text{Co}$ bilayers (see Supplementary Materials) [18, 20]. FC and zero-field cooled (ZFC) measurements of M vs. T of all alloy samples behaved in a way that can be explained by the appearance of a ferromagnetic multi-domain state during the ZFC process and its realignment after field-cooling (see Fig. 2 inset).

TRM data in Fig. 1 show the general effect of alloying on M . Relatively small deviations of x from the pure phases result in significant increases of M at low T , but these values are much smaller than would be expected for ferrimagnetic order [23], and are therefore due to magnetic disorder.

Examples of TRM phase transitions with $H_{FC} \parallel c$ -axis, and $H_{FC} \perp c$ -axis for the $x = 0.0$ sample, are shown in Fig. 2(a). The TRM data for all alloy samples had an inflection at a lower T than the actual onset of the remanent magnetization, while the pure FeF_2 and NiF_2 samples only had one transition. The fits to the data using Eq. 3 with two transitions for the alloys and one transition for the pure samples, indicated that $\beta \approx 0.34 \pm 0.05$ for all samples. The transition temperatures and transition widths obtained from the fits for all samples are shown in Fig. 4 and discussed further below. The presence of two phase transitions was more clearly seen in the form of two minima, at $T = T_1$ and $T = T_2$, in the $\partial M / \partial T$ vs. T data, as shown in Fig. 2(b). When the TRM was measured in small H applied along the c-axis, the transition at T_2 broadened substantially, while the transition at T_1 and the low temperature TRM remained unaffected. This phenomenon occurred for all samples with $0.2 < x < 1.0$. For $x = 0.1$, a similar transition was observed with $H \perp c$, indicating the existence of the easy-plane ordering similar to that of pure NiF_2 . TRM data for $H \parallel c$ had unusual behavior due to the existence of an oblique phase, as discussed below (see Supplementary Materials).

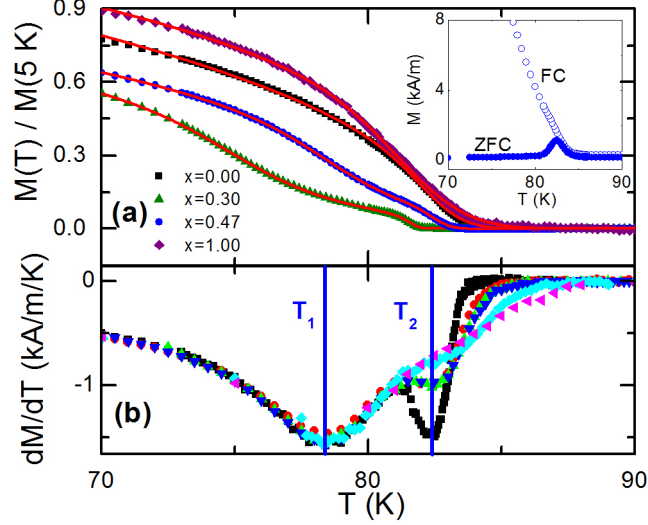


FIG. 2. (a) TRM data ($H = 0$) near the phase transition for four representative samples. Symbols are data and red curves are fits to Eq. 3 with two transitions for $x = 0.30, 0.47$ and one transition for $x = 1.0$ and $x = 0.0$. Inset: M measured while warming with $H = 80$ Oe applied along the c -axis after ZFC from $T = 300$ K to 5 K and during FC from 300 K to 5 K for the $x = 0.47$ sample. (b) Numerical derivative $\partial M/\partial T$ of the $x = 0.47$ TRM data measured under different applied fields. Vertical blue lines indicate transition temperatures T_1 and T_2 .

The magnetic phase in the range $T_1 < T < T_2$, where the magnetic structure is strongly coupled to H , can be explained in two ways: (1) there is a first order spin-reorientation transition from an Ising-like, single-axis anisotropy structure, similar to FeF_2 , to a weakly ferromagnetic structure, similar to NiF_2 , at $T = T_1$ with increasing T , or (2) the transition at $T = T_1$ is from the FeF_2 magnetic structure to a magnetically disordered structure. In order to determine which of these explanations is correct, neutron scattering was measured in $x = 0.1$ and $x = 0.3$ 100 nm thick samples using 3.0 and 3.4 meV neutron beams from the cold neutron triple-axis spectrometer (CTAX) at the High Flux Isotope Reactor, Oak Ridge National Laboratory (see Supplementary Materials for more details). Prior to measurement, the samples were cooled in $H_{FC} = 60$ Oe \parallel c -axis. Once cooled to $T = 4$ K, H was removed and the integrated intensities of the magnetic (100) and (001) reflections with their background subtracted, $I_{(100)}$ and $I_{(001)}$ (corresponding nuclear reflections are forbidden), were measured as a function of increasing T . From neutron scattering selection rules, $I_{(100)} \propto L_c^2 + L_b^2$, where $L_{b,c}$ is the component of the staggered magnetization vector \mathbf{L}

of the AF along the c- or b-axis, while $I_{(001)} \propto L_{ab}^2$, where $L_{ab}^2 = L_a^2 + L_b^2$ is the component of \mathbf{L} in the $a - b$ plane. The staggered magnetization vector is defined by $\mathbf{L} = (\mathbf{M}_1 - \mathbf{M}_2)$, where $\mathbf{M}_{1,2}$ are the two sublattice magnetization vectors with $M_1 = M_2$. Explanation (1) would result in $I_{(001)} \neq 0$ only in the $T_1 < T < T_2$ temperature range. On the other hand, explanation (2) requires that $I_{(100)}, I_{(001)} > 0$ only for $T < T_1$ because lack of long-range order in the $T_1 < T < T_2$ range would preclude the observation of magnetic scattering.

Figure 3(a) shows $I_{(100)}(T)$ and $I_{(001)}(T)$. For both samples, the data indicate the presence of a single phase transition. For the $x = 0.3$ sample, $I_{(001)} = 0$ for $0 < T < 85$ K, and therefore the spins did not order antiferromagnetically in the a-b plane. For the $x = 0.1$ sample, both $I_{(100)}$ and $I_{(001)}$ were non-zero at low T , and both $\rightarrow 0$ as $T \rightarrow T_1$. This indicates that \mathbf{L} pointed in an oblique direction between the c-axis and the a-b plane. Fitting the data to a rounded power law phase transition similar to Eq. 3, but with $\beta \rightarrow 2\beta$ to take into account the fact that $I \propto L^2$, yielded the results shown in Fig. 3(b). The value of T_N coincided with T_1 measured for $x = 0.1$ and $x = 0.3$ samples within uncertainties. Because no significant intensity was observed for $T > T_N \approx T_1$ for either sample, we conclude that explanation (2) is correct: there is a transition with increasing T from an AF with long-range order to a disordered magnetic phase in the $T_1 < T < T_2$ range.

The values of β from neutron scattering agreed with those from the TRM measurements. They are in better agreement with critical exponents corresponding to the 3D Ising, Heisenberg, and random exchange models ($\beta \approx 0.35$) [16] than with the 3D random field model ($\beta \sim 0.1$) [21, 24, 25]. To determine β more accurately, and thus identify the transition's universality class, measurements must be made of the lineshape as a function of scattering wavevector, T and H to take into account possible incoherent scattering backgrounds common in random magnetic systems [21, 24]. Significantly thicker samples than the ones used here, possibly bulk single crystals, would be required. Accurately determining the universality class is therefore beyond the scope of this paper.

Whereas $L_{a-b} = 0$ for the $x = 0.3$ sample throughout the entire T range, this is not the case for the $x = 0.1$ sample. This means that for $x = 0.1$ an oblique phase exists throughout most, if not the entire T range, where \mathbf{L} points at an angle θ away from the c-axis. The value of θ can be determined using $L^2 = L_c^2 + L_{ab}^2$ and assuming that $L_b = L_a$, i.e., oblique domains are equally likely to tilt towards the a- or b-axis, which yields $\tan \theta = \left(I_{(001)} / I_{(100)} - 1/2 \right)^{1/2}$. The dependence of θ on T calculated from this equation is shown in Fig. 3(c).

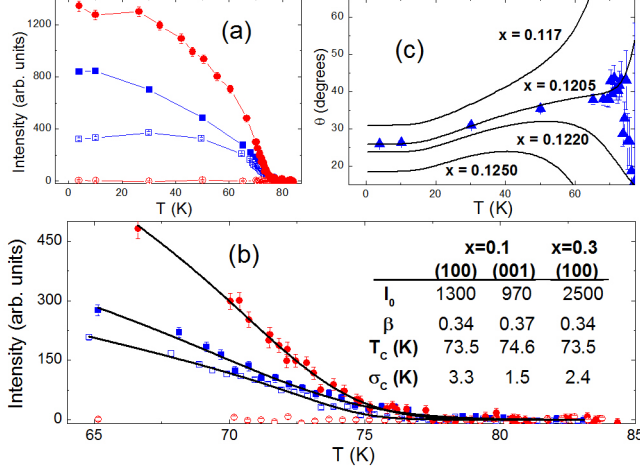


FIG. 3. (a) Neutron scattering intensity as a function of temperature for the $x = 0.3$ (red circles) and $x = 0.1$ samples (blue squares). Filled and open symbols indicate (100) and (001) reflections, respectively. Lines are guides to the eye. (b) Intensity near T_c . Black curves are fits to Eq. 3 (with $\beta \rightarrow 2\beta$) and the resulting fitting parameters are shown in the graph. (c) Angle of the staggered magnetization vector \mathbf{L} as a function of T with respect to the c -axis for the $x = 0.1$ sample calculated from the data in (a). The solid curves are calculations using MFT for the values of x indicated in the graph.

The phase diagram in Fig. 4, constructed from the TRM and neutron scattering data, can be understood using mean field theory (MFT). While MFT is inaccurate when predicting T_N , it is relatively successful at predicting quantities which depend on changes in the effective field rather than on its absolute value [26] and can describe, at least qualitatively, the concentration dependence of T_N in mixed AF systems [27]. The spin Hamiltonian included single-ion anisotropy terms and Heisenberg-type exchange contributions, similar to the model used by Moriya [17] to study weak ferromagnetism in NiF_2 . Using mean field decoupling for the exchange interactions while treating the single-site anisotropy terms exactly yields an average of the η spin component for α -type ions (either Fe or Ni) on the sublattice λ

$$\langle S_\alpha^\eta \rangle_\lambda = \frac{1}{Z_{\alpha\lambda}} \text{Tr} [S_\alpha^\eta \exp(-H_{\alpha\lambda}/k_B T)], \quad (4)$$

where the effective single-site Hamiltonian has the form

$$H_{\alpha\lambda} = \sum_\eta \tilde{h}_{\alpha\lambda}^\eta S_\alpha^\eta + D_\alpha (S_\alpha^Z)^2 \quad (5)$$

with the molecular field given by

$$h_{\alpha\lambda}^{\approx\eta} = z \sum_{\beta=\text{Ni,Fe}} J_{\alpha\beta} p_{\beta} \langle S_{\beta}^{\eta} \rangle_{\lambda}. \quad (6)$$

In Eq. 4 the partition function is $Z_{\alpha\lambda} = \text{Tr} [\exp(-H_{\alpha\lambda}/k_B T)]$ and the spins S_{α}^{η} are represented by 3×3 and 5×5 matrices for Ni and Fe ions, respectively. At a given T , $\langle S_{\alpha}^{\eta} \rangle_{\lambda}$ was determined numerically using an iterative scheme. Convergence was checked in the limit $D_{\alpha} = 0$ by comparing with analytic expressions obtained within the full decoupling scheme (see Supplementary Materials for more details). The exchange coupling constants $J_{\alpha_j\beta_k}$ were non-zero for next-nearest neighbor sites j and k (between ions at the center of the tetragonal unit cell with those at the corners) and could take the values J_{NiNi} , J_{FeFe} , and J_{NiFe} , corresponding to the different possible pairs of spins. Weaker exchange contributions with other neighbors were neglected. The number of interacting neighbors was $z = 8$ and D_{α} was positive for Ni ions and negative for Fe ions. Self-consistent calculations were carried out until the upper end of the phase diagram in Fig. 4 was reproduced.

Results of MFT calculations are shown in Fig. 4. The paramagnet (PM)-AF phase transition boundary was reproduced by adjusting the exchange constants to $J_{\text{FeFe}} = 0.475$ meV, $J_{\text{NiNi}} = 1.63$ meV, and $J_{\text{NiFe}} = 0.94$ meV, and using the known single-ion anisotropy constants $D_{\text{Fe}} = -0.80$ meV and $D_{\text{Ni}} = 0.54$ meV [15, 28]. T_N values for pure NiF_2 and FeF_2 samples were larger than expected from the bulk parameters, but this has been previously attributed to strain (piezomagnetism) [29, 30]. The exchange constants were therefore different than the bulk values ($J_{\text{FeFe}} = 0.451$ meV and $J_{\text{NiNi}} = 1.72$ meV) [15, 28]. This non-monotonic dependence of T_2 on x is due to an enhancement of the exchange between unlike ions, $J_{\text{FeNi}} = 0.88$ meV $> \sqrt{J_{\text{FeFe}} J_{\text{NiNi}}}$, similar to what has been observed in $\text{Fe}_x\text{Mn}_{1-x}\text{F}_2$ [26]. Increasing J_{NiFe} much further shifts the minimum to $x = 0$.

MFT also predicts a region where oblique ordering occurs, similar to prior MFT results for AF systems with anisotropic exchange couplings [4, 6]. The canting angle $\theta(T)$ was calculated using the same model and is depicted by the black curves in Fig. 3(c) (see SM). The behavior was found to be extremely sensitive to x and remarkably good agreement was found for $x \sim 0.1205$, which is consistent with the sample's nominal concentration of $x = 0.1 \pm 0.05$, but with $J_{\text{NiFe}} = 1.02$ meV. This indicates that other exchange interactions neglected by the model may play a role in determining $\theta(T)$.

Regions of different types of order predicted by the calculations are indicated in Fig. 4.

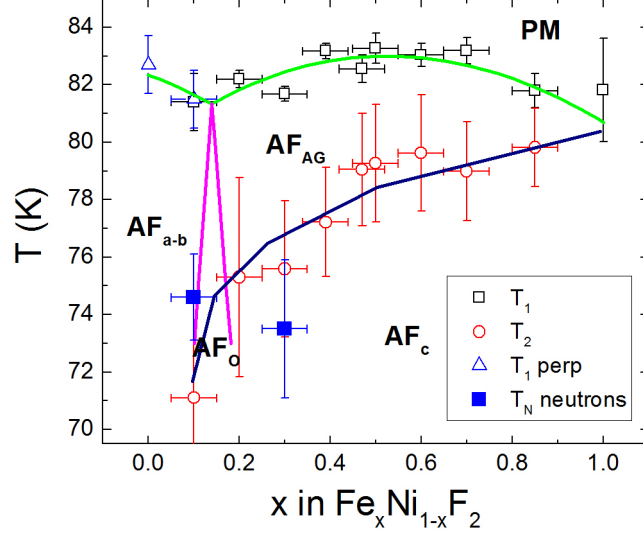


FIG. 4. Magnetic phase diagram for $\text{Fe}_x\text{Ni}_{1-x}\text{F}_2$. Regions are indicated by AF_{a-b} (ordering in the a - b plane), AF_c (ordering along the c -axis), AF_{AG} (anisotropy glass phase), AF_O (oblique phase), and PM (paramagnetic phase). The PM-AF phase boundary calculated using MFT is denoted by the solid green curve. T_1 and T_2 were determined from fits to Eq. 3 of TRM data. Horizontal error bars represent uncertainty in x from quartz crystal monitor measurements. Vertical error bars correspond to the transition widths σ_{T_C} . Measurements taken for samples that had a response with $H \perp$ to the c -axis ($[\bar{1}10]$ direction, \triangle) are also indicated. Magenta lines enclose the MFT AF_O region. Transitions observed via neutron scattering are also indicated. The dark blue curve is a AF_c - AF_{AG} phase boundary drawn as a guide to the eye.

Whereas the calculated PM/AF boundary agrees well with T_2 , neutron scattering data indicate that long-range order disappears for $T > T_1$. This leads to the conclusion that a Griffiths-like [31–33] short-range order phase exists in the $T_1 < T < T_2$ region as a result of the random single-ion anisotropy. Griffiths phases in other AFs usually result from frustration of their exchange interactions. For example, magnetic field-induced antiferromagnetic correlations have been reported in metamagnetic FeCl_2 [34], in intraplanar frustrated FeBr_2 [35], and in the dilute AFs $\text{Fe}_{1-x}\text{Zn}_x\text{F}_2$ [36] and $\text{Rb}_2\text{Co}_{1-x}\text{Mg}_x\text{F}_4$ [37]. Here we propose a mechanism where a breakdown of magnetic long-range order occurs at T_1 , with the random orthogonal single-ion magnetic anisotropy playing the role of an effective local random field that leads to frustration. The emerging RMA-induced anisotropy glass region exists in the interval $T_1 < T < T_2$, where T_2 is the upper phase transition determined by the average

exchange interaction strength of the alloy. The MFT used here is unable to reproduce this region because it does not take into account local fluctuations of the effective field.

In conclusion, the magnetic structure of $\text{Fe}_x\text{Ni}_{1-x}\text{F}_2$, an authentic 3D AF with random single-ion magnetic anisotropy, transforms from easy a-b plane to the easy c-axis with increasing x via an oblique phase region at $x = 0.10-0.14$. Two phase transition temperatures, T_1 and T_2 , were identified for $0.2 < x < 0.9$. Long-range order disappears for $T > T_1$, but short-range order persists up to $T = T_2$. The short-range order region is a result of the RMA which induces a magnetic glass phase for $T_1 < T < T_2$. This phase is similar to magnetic glassy states formed as a result of combining structural disorder with frustrated exchange interactions, but with randomly distributed single-ion anisotropies replacing exchange frustration as the driving mechanism. These effects have not been observed before in AFs because most AF systems studied to date do not have authentic single-ion RMA, but rather have an effective RMA induced by asymmetric exchange interactions which decreases rapidly as T_N is approached.

The supports of the National Science Foundation (grant No. DMR-0903861) and the WV Higher Education Policy Commission (Research Challenge Grant HEPC.dsr.12.29) at WVU are gratefully acknowledged. Some of the work was performed using the WVU Shared Research Facilities. Research conducted at ORNL and LANL was sponsored by the Scientific User Facilities Division, Office of Basic Energy Sciences, US Department of Energy.

* Current address: Integrated Microscopy Center, The University of Memphis, Memphis, TN 38152.

† david.lederman@mail.wvu.edu

- [1] D. S. Fisher, G. M. Grinstein, and A. Khurana, *Physics Today* **41**, 56 (1988).
- [2] P. Wong, P. M. Horn, R. J. Birgeneau, and G. Shirane, *Phys. Rev. B* **27**, 428 (1983).
- [3] W.A.H.M. Vlak, E. Frikee, A.F.M. Arts, and H.W. de Wijn, *Phys. Rev. B* **33**, 6470 (1986).
- [4] F. Matsubara and S. Inawashiro, *J. Phys. Soc. of Japan* **42**, 1529 (1977).
- [5] S. Fishman and A. Aharony, *Phys. Rev. B* **18**, 3507 (1978).
- [6] F. Matsubara and S. Inawashiro, *J. Phys. Soc. of Japan* **46**, 1740 (1979).
- [7] M. K. Wilkinson, J. W. Cable, E. O. Wollan, and W. C. Koehler, *Phys. Rev.* **113**, 497 (1959).

- [8] T. Tawaraya and K. Katsumata, *Solid State Commun.* **32**, 337 (1979).
- [9] T. Tawaraya, K. Katsumata, and H. Yoshizawa, *J. Phys. Soc. Jpn.* **49**, 1299 (1980).
- [10] P. Wong, P. M. Horn, R. J. Birgeneau, C. R. Safinya, and G. Shirane, *Phys. Rev. Lett.* **45**, 1974 (1980).
- [11] K. Katsumata, J. Tuchendler, and S. Legrand, *Phys. Rev. B* **30**, 1377 (1984).
- [12] Q. J. Harris, Q. Feng, Y. S. Lee, R. J. Birgeneau, and A. Ito, *Phys. Rev. Lett.* **78**, 346 (1997).
- [13] K. Haefner, J. W. Stout, and C. S. Barrett, *J. Appl. Phys.* **37**, 449 (1966).
- [14] W. Jauch, A. Palmer, and A. J. Schultz, *Acta Cryst. B* **49**, 984 (1993).
- [15] M. T. Hutchings, M. F. Thorpe, R. J. Birgeneau, P. A. Fleury, and H. J. Guggenheim, *Phys. Rev. B* **2**, 1362 (1970).
- [16] D. Belanger and H. Yoshizawa, *Phys. Rev. B* **35**, 4283 (1987).
- [17] T. Moriya, *Phys. Rev.* **117**, 635 (1960).
- [18] M. Cheon, Z. Liu, and D. Lederman, *Appl. Phys. Lett.* **90**, 012511 (2007).
- [19] M. R. Fitzsimmons, D. Lederman, M. Cheon, H. Shi, J. Olamit, I. V. Roshchin, and I. K. Schuller, *Phys. Rev. B* **77**, 224406 (2008).
- [20] M. Cheon, Z. Liu, and D. Lederman, *J. Appl. Phys.* **101**, 09E503 (2007).
- [21] R. J. Birgeneau, *J. Magn. Magn. Mater.* **177-181**, 1 (1998).
- [22] D. Lederman, J. Nogués, and I. K. Schuller, *Phys. Rev. B* **56**, 2332 (1997).
- [23] T. Tsushima, T. Teranishi, and K. Ohta, Handbook on magnetic substances (Asakura Publishing Co., Tokyo, 1975).
- [24] D. Belanger and A. Young, *J. Magn. Magn. Mater.* **100**, 272 (1991).
- [25] F. Ye, L. Zhou, S. Larochelle, L. Lu, D. P. Belanger, M. Greven, and D. Lederman, *Phys. Rev. Lett.* **89**, 157202 (2002).
- [26] G. K. Wertheim, H. J. Guggenheim, M. Butler, and V. Jaccarino, *Phys. Rev.* **178**, 804 (1969).
- [27] Z. Néda, *Phys. Rev. B* **50**, 3011 (1994).
- [28] M. T. Hutchings, B. D. Rainford, and H. J. Guggenheim, *J. Phys. C: Solid State Phys.* **3**, 307 (1970).
- [29] J. Mattsson, C. Djurberg, and P. Nordblad, *J. Magn. Magn. Mater.* **136**, L23 (1994).
- [30] H. Shi, D. Lederman, K. V. O'Donovan, and J. A. Borchers, *Phys. Rev. B* **69**, 214416 (2004).
- [31] R. B. Griffiths, *Phys. Rev. Lett.* **23**, 17 (1969).
- [32] B. McCoy, *Phys. Rev. Lett.* **23**, 383 (1969).

- [33] T. Vojta, *J. Phys. A: Math. Gen.* **39**, R143 (2006).
- [34] C. Binek and W. Kleemann, *Phys. Rev. Lett.* **72**, 1287 (1994).
- [35] C. Binek, M. de Azevedo, W. Kleemann, and D. Bertrand, *J. Mag. Magn. Mater.* **140–144**, 1555 (1995).
- [36] C. Binek, S. Kuttler, and W. Kleemann, *Phys. Rev. Lett.* **75**, 2412 (1995).
- [37] C. Binek, W. Kleemann, and D. P. Belanger, *Phys. Rev. B* **57**, 7791 (1998).